

Distribution of Earth's radiation belts protons over the drift frequency of particles

Alexander S. Kovtyukh

Skobeltsyn Institute of Nuclear Physics, Moscow State University, Moscow, 119234, Russia

Correspondence: Alexander S. Kovtyukh (kovtyukhas@mail.ru)

Abstract. Thanks to the data on the proton fluxes of the Earth's radiation belts (ERB) with energy ranging from 0.2 to 100 MeV and drift L shells ranging from 1 to 8, their stationary distributions over the drift frequency f_d of protons around the Earth are constructed. For this purpose, direct measurements of proton fluxes of the ERB in the period 1961–2017 near the geomagnetic equator were employed. The main physical processes in the ERB manifested more clearly in these distributions, and for protons with $f_d > 0.5$ mHz at $L > 3$ their distributions in the space $\{f_d, L\}$ have a more regular shape than in the space $\{E, L\}$. The main physical processes in the ERB manifested more clearly in these distributions, and for protons with $f_d > 0.5$ mHz at $L > 3$ distributions of the ERB protons in the space $\{f_d, L\}$ have a more orderly form than in the space $\{E, L\}$. It has been found also that the quantity of the ERB protons with $f_d \sim 1$ –10 mHz at $L \sim 2$ does not decrease, as for protons with $E > 10$ –20 MeV (with $f_d > 10$ mHz), but increases with an increase in solar activity. This means that the balance of radial transport and losses of the ERB low-energy protons at $L \sim 2$ is disrupted in advantage of transport: for these protons, the effect of an increase in the radial diffusion rates with increasing solar activity, overpowers the effect of an increase in the density of the dissipative medium.

Keywords. Magnetospheric physics (energetic particles, trapped). Radiation belts.

25 1 Introduction

26 The Earth's radiation belts (ERB) consist mainly of charged particles with energy from $E \sim 100$
 27 keV to several hundreds of megaelectronvolt (MeV). In the field of the geomagnetic trap, each
 28 particles of the ERB with energy E and equatorial pitch-angle α_0 (α is the angle between the local
 29 vector of the magnetic field and the vector of a particle velocity) makes three periodic movements:
 30 Larmor rotation, oscillations along the magnetic field line, and drift around the Earth (Alfvén and
 31 Fälthammar, 1963; Northrop, 1963).

32 Three adiabatic invariants (μ , K , Φ) correspond to these periodic motions of trapped particles,
 33 as well as three periods of time or three frequencies: a cyclotron frequency f_c , a frequency of
 34 particle oscillations along the magnetic field line f_b , and a drift frequency of particles around the
 35 Earth f_d . For the near-equatorial ERB protons, we have: $f_c \sim 1\text{--}500$ Hz, $f_b \sim 0.02\text{--}2$ Hz and $f_d \sim 0.1\text{--}$
 36 20 mHz. The frequency f_c increases by tens to hundreds of times with the distance of the particle
 37 from the plane of the geomagnetic equator (in proportion to the local induction of the magnetic
 38 field), and the frequency f_b decreases by almost 2 times with increasing amplitude of particles
 39 oscillation.

40 The number of particles with a given frequency f_c decreases rapidly with an increase of L , and
 41 refers to higher and higher geomagnetic latitudes. For each given value of a frequency f_b , particles
 42 become more and more energetic with an increase of L ($E \propto L^2$) and their number becomes
 43 smaller.

44 Compared to the frequencies f_c and f_b , the drift frequency f_d for one particle species has a much
 45 narrower range of values; it does not depend on the mass of the particles and it very weakly
 46 depends on the amplitude of their oscillations (vary within $\sim 20\%$); in this case, on each L -shell
 47 there are a significant number of particles corresponding to a certain value of f_d .

48 Therefore, it can be expected that the distributions of the ERB particles in the space $\{f_d, L\}$ will
 49 have a more regular shape than in the space $\{E, L\}$, and the main physical processes in these belts
 50 will manifest themselves more clearly in these distributions. Furthermore, it can also be expected
 51 that on these more ordered background more fine features can be revealed that would not appear in
 52 the space $\{E, L\}$.

53 Despite the importance of the drift frequency f_d for the mechanisms of the ERB formation,
 54 reliable and sufficiently complete distributions of particles in the ERBs (over the frequency f_d)
 55 have not been presented nor analyzed; indeed, this is the first time.

56 The analysis presented in this paper is limited to the protons of the ERB during magnetically
 57 quiet periods of observations, when the proton fluxes and their spatial-energy distributions were
 58 stationary. In the following sections, the distributions of the ERB protons over their drift
 59 frequency f_d are constructed from experimental data (Sect. 2), and analyzed (Sect. 3). Finally, the
 60 main conclusions of this work are given in Sect. 4.

61 2 Constructing the distributions of the ERB protons over their drift frequency

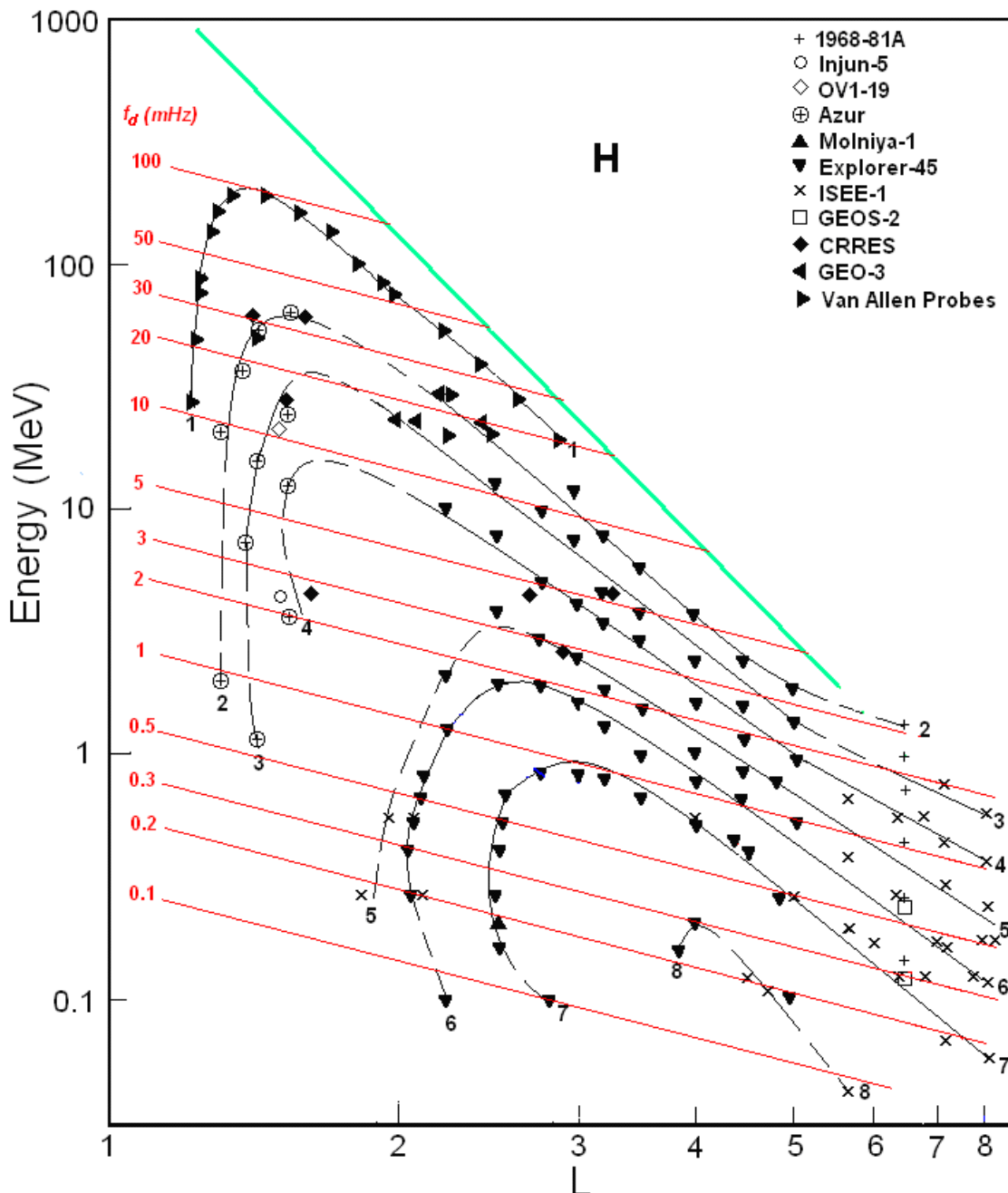
62 2.1 Spatial-energy distributions of the ERB protons near the equatorial plane

63 To construct the distributions of the ERB particles over the drift frequency, it is necessary to have
 64 reliable distributions of the differential fluxes of the ERB protons in the space $\{E, L\}$, where E is
 65 the kinetic energy of protons and L is the drift shell parameter.

66 From the data of averaged satellite measurements of the differential fluxes of protons with an
 67 equatorial pitch-angle $\alpha_0 \approx 90^\circ$, aforementioned distributions are constructed in (Kovtyukh, 2020)

68 during quiet periods. Such distributions, separately between periods near minima and maxima of
 69 the 11-year solar activity cycle, are constructed from satellite data also for other ionic components
 70 of the ERB (near the equatorial plane), but the most reliable and detailed picture was obtained in
 71 for protons (see Kovtyukh, 2020). In Fig. 1 one of these distributions is reproduced for periods
 72 near solar maxima (from 1968 to 2017); here, data of different satellites are associated with
 73 different symbols.

74 The numbers on the curves (iso-lines) refer to the values of the decimal logarithms of the
 75 differential fluxes J ($\text{cm}^2 \text{ s sr MeV}^{-1}$) of protons (with equatorial pitch-angle $\alpha_0 \approx 90^\circ$). The red
 76 lines in Fig. 1 correspond to the dependences $f_d(\text{mHz}) = 0.379 \cdot L \cdot E(\text{MeV})$ for the drift frequency of
 77 the near-equatorial protons in the dipole approximation of the geomagnetic field.



78

79 **Figure 1.** Distribution of the differential fluxes $J(E, L)$ in the space $\{E, L\}$ for protons with $\alpha_0 \approx 90^\circ$ near maxima of
 80 the solar activity (Kovtyukh, 2020). Data of satellites are associated with different symbols. The numbers on the

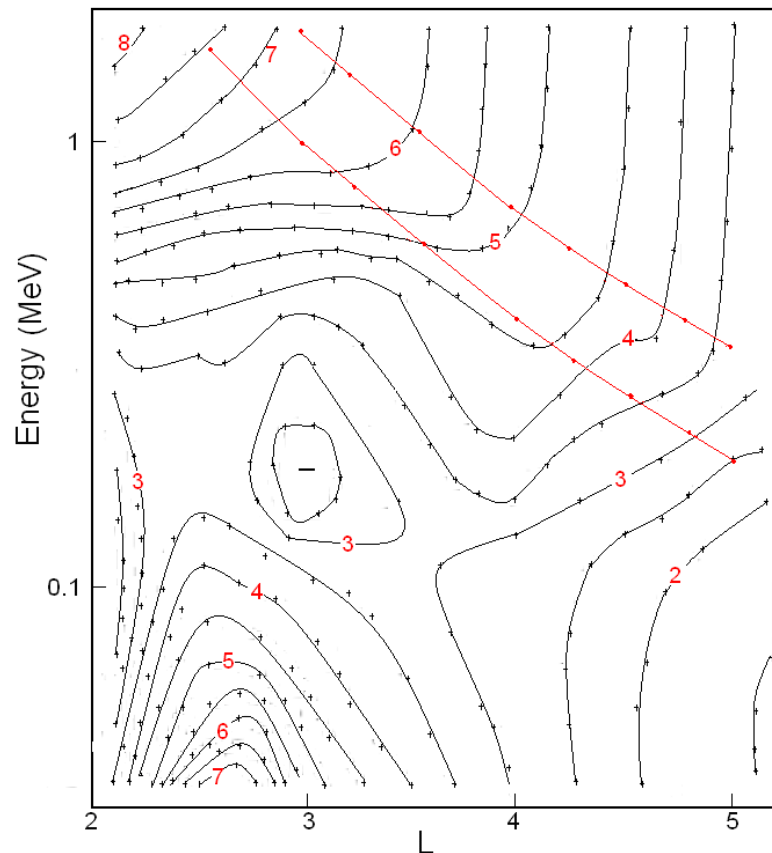
81 curves refers to the values of the decimal logarithms of J . Fluxes is given in units of $(\text{cm}^2 \text{ s sr MeV})^{-1}$. The red lines
 82 correspond to the drift frequency f_d (mHz). The green line corresponds to the maximum energy of the trapped protons.

83 Only protons with energies less than some maximum values, determined by the Alfvén's
 84 criterion: $\rho_c(L, E) \ll \rho_B(L)$, where ρ_c is the gyroradius of protons, and ρ_B is the radius of curvature
 85 of the magnetic field (near the equatorial plane) **can be trapped on the drift shells**. According to
 86 this criterion and to the theory of stochastic motion of particles, the geomagnetic trap in the dipolar
 87 region can capture and durably hold only protons with E (MeV) $< 2000 \cdot L^{-4}$ (Ilyin et al., 1984). The
 88 green line in Fig. 1 represents this boundary.

89 The distribution of the ERB proton fluxes shown in Fig. 1, refers to the years of the solar
 90 maximum, but the solar-cyclic variations in the ERB proton fluxes are small and localized at $L <$
 91 2.5 (mainly at $L < 1.4$).

92 2.2 Spatial-energy distributions of the ERB protons outside the equatorial plane

93 The stationary fluxes J of the ERB particles with given energy and local pitch-angle α decrease
 94 usually when the point of observation is shifted from the equatorial plane to higher latitudes along
 95 a certain magnetic field line. In the inner regions of the ERB, on $L < 5$, an angular distributions of
 96 protons have usually a maximum at the local pitch-angle $\alpha = 90^\circ$. In wide interval near this
 97 maximum these distributions are well described by the function
 98 $J(\alpha, B/B_0) \propto (B/B_0)^{-A/2} \sin^A \alpha$ (Parker, 1957), where A is the index of an anisotropy of a
 99 fluxes, B is the induction of a magnetic field at the point of measurements of these fluxes and B_0 is
 100 induction of a magnetic field at the equatorial plane on the same magnetic line.



102 **Figure 2.** Empirical model of the anisotropy index $A(E, L)$ of the ERB proton fluxes averaged on the data of the
 103 satellites obtained near the plane of the geomagnetic equator. Values of A are given on iso-lines of the anisotropy: $A =$
 104 1.5–8.5 with the step $\Delta A = 0.5$.

105 The empirical model of an anisotropy $A(E, L)$ for the proton fluxes with $E \sim 0.1$ –2 MeV on $L \sim$
 106 2–5 near the equatorial plane for the stationary ERB ($Kp < 2$) is presented in Fig. 2. The anisotropy
 107 index A of these fluxes is shown in Fig. 2, in the space $\{E, L\}$, in the form of iso-lines with the
 108 same values A from 1.5 to 8.0 and with a step $\Delta A = 0.5$. The integer values of this index are plotted
 109 on the corresponding iso-lines as red numbers.

110 When constructing this model, we consider and analyze the data of the following satellites:
 111 Explorer-12 (Hoffman and Bracken, 1965), Explorer-14 (Davis, 1965), Explorer-26 (Søraas and
 112 Davis, 1968), OV1-14 and OV1-19 (Fennell et al., 1974), Explorer-45 (Williams and Lyons, 1974;
 113 Fritz and Spjeldvik, 1981; Garcia and Spjeldvik, 1985), ISEE-1 (Garcia and Spjeldvik, 1985;
 114 Williams and Frank, 1984), SCATHA (Blake and Fennell, 1981), Van Allen Probes (Shi et al.,
 115 2016), and other satellites. These data were obtained in 1961-2015.

116 Fig. 2 shows that for rather high energy (> 1 MeV) the anisotropy of a proton fluxes
 117 monotonically increases with decreasing L (from $A \sim 3.5$ to $A \sim 8.0$). For $E > 0.3$ MeV on $L < 3$
 118 anisotropy is monotonically increases with increasing energy, but for $E > 0.5$ MeV on $L > 3$ it is
 119 almost energy-independent.

120 Some small irregularities of the iso-lines in Fig. 2 are due to the fact that experimental data
 121 were used for constructing this figure; these data were obtained in different years, with different
 122 instruments on different orbits of satellites, and during different intensity of the solar activity. At
 123 the same time, Fig. 2 demonstrates the important regularities of the pitch-angle distributions of the
 124 stationary ERB protons.

125 In the region $\{E > 0.5$ MeV, $L > 3\}$ the iso-lines of the anisotropy index are almost parallel to
 126 each other and to the energy axis. This adiabatic regularity refers to protons belonging to the
 127 power-law tail of their energy spectra, the exponent of which practically does not change when L
 128 changes (at $L > 3$). In Fig. 2, the red lines correspond to the lower boundary of the power-law tail
 129 of the ERB protons energy spectra: $E_b = (36 \pm 11) L^{-3}$ MeV (see Kovtyukh, 2001, 2020).

130 The pattern of $A(E, L)$ in the region on $L > 3$ at $E \sim 0.2$ –0.5 MeV and the local minimum at $L \sim$
 131 3 ($E \sim 0.2$ MeV) are connected with local maximum in the stationary proton energy spectra of the
 132 ERB which corresponds to $E = (17 \pm 3) L^{-3}$ MeV (see Kovtyukh, 2001, 2020).

133 These regularities in the pattern of $A(E, L)$ are explained within the framework of the theory of
 134 radial transport (diffusion) of the ERB protons with conservation of the adiabatic invariants μ and
 135 K of their periodic motions (these issues were most fully considered in Kovtyukh, 1993).

136 Both the local maximum at $L \sim 2.5$ ($E < 0.1$ MeV) and the region of low anisotropy at $L \sim 2$ (E
 137 ~ 0.1 MeV) in Fig. 2, are related to the ionization losses of protons.

138 On the data of the satellites, the pitch-angle distributions of the ERB proton fluxes strongly
 139 depend on MLT at $L > 5$: the average index A values on the day side are larger than on the night
 140 side, and this dependence becomes more distinct with increasing energy (see, e.g., Shi et al., 2016).
 141 These results indicate that drift shells splitting (see Roederer, 1970) play an important role in the
 142 formation of these distributions at $L > 5$. In the calculations performed here, it was assumed that
 143 near the equatorial plane the pitch-angle distributions of the ERB proton fluxes at $L > 6$, averaged
 144 over MLT, at $\alpha_0 \sim 90^\circ$ are nearly isotropic.

145 High anisotropy for the fluxes of protons at $E = 5$ –50 MeV and a strong dependence $A(L)$ at the
 146 inner boundary of the inner belt ($L = 1.15$ –1.40, $B/B_0 = 1.0$ –1.7) were obtained on the satellite
 147 DIAL (Fischer et al., 1977). According to these data, an anisotropy index increase from $A \sim 12$ at
 148 $L = 1.25$ to $A \sim 60$ at $L = 1.15$, and do not depends on L at $L = 1.25$ –1.40. These results are supported

149 by the data of the satellite Resurs-01-N4 for the protons with $E = 12\text{--}15$ MeV which were
 150 obtained at $h \sim 800$ km (Leonov et al., 2005). These results are taken into account in our
 151 calculations.

152 The experimental results on the pitch-angle distributions of the ERB proton fluxes and their
 153 anisotropy indexes were discussed in detail in (Kovtyukh, 2018).

154 2.3 Drift frequency distributions of the ERB protons

155 Based on the results shown in Fig. 1 and 2, one can calculate the distributions of the ERB protons
 156 over the drift frequency f_d . In these calculations, the dipole model of the geomagnetic field was
 157 used, according to which (see, e. g., Roederer, 1970) the point of the magnetic field line at
 158 geomagnetic latitude λ is located from the center of the dipole at a distance

$$159 \quad R(L, \lambda) = R_E L \cos^2 \lambda,$$

160 where R_E is the Earth's radius, and the field induction at a given L changes with changing λ as

$$161 \quad B(L, \lambda) = \frac{\sqrt{4 - 3 \cos^2 \lambda}}{\cos^6 \lambda} B_0(L),$$

162 where $B_0(L) = 0.311 \text{ G} \times L^{-3}$.

163 It was also taken into account that the drift frequency f_d of the nonrelativistic particles depends
 164 essentially only on their kinetic energy E and on L . This value depends very slightly on the particle
 165 pitch-angle: with an increase in the geomagnetic latitude of the mirror point of the particle trajectory
 166 from 0 to 10° , it increases by only 1.5%, and in the range from 0 to $20\text{--}30^\circ$ it increases by 5.8–12.5%.

167 The number of protons with energies from E to $E+dE$ per unit volume n is equal to the differential
 168 flux of these particles J (falling per unit time per unit area of the detector per unit solid angle), divided
 169 by the velocity v of these particles: $n = J/v$. For nonrelativistic protons with mass m , this velocity is
 170 $(2E/m)^{1/2}$.

171 Then in the near-equatorial region, between L and $L+dL$ and within geomagnetic latitudes from
 172 0 to $\pm\lambda_0$, the total number of nonrelativistic protons with mirror points within this region and with
 173 energy from E to $E+dE$, drifting on a given L with frequency $f_d(L, E)$ around the Earth, is

$$174 \quad \Delta N(L, f_d) = 2 \int_0^{\lambda_0} 2\pi R_E^2 L dL \frac{B_0(L)}{B(L, \lambda)} R_E L \cos \lambda \sqrt{4 - 3 \cos^2 \lambda} d\lambda \times$$

$$4\pi \int_{\alpha_{01}}^{\alpha_{02}} \frac{J(L, E(L, f_d)) dE}{\sqrt{2E(L, f_d)/m}} \sin^A \alpha_0 \cos \alpha_0 d\alpha_0,$$

175 where m is the rest mass of a proton, $J(L, E(L, f_d))$ is the differential fluxes and $E(L, f_d)$ is the protons
 176 energy. The first integral takes into account that the magnetic flux in the layer between shells L and

177 $L+dL$ it conserved when latitude λ changes, i. e. $2\pi R_E L \cos \lambda R_E dL = 2\pi R_E L \frac{B_0(L)}{B(L, \lambda)} R_E dL$.

178 As result of integrating the last expression over α_0 and replacing $\cos \lambda \equiv t$, we obtain:

$$\Delta N(L, f_d) = 4\pi R_E^3 L^2 dL \frac{J(L, E(L, f_d)) dE}{\sqrt{2E(L, f_d)/m}} \times \frac{4\pi}{A+1} \times$$

$$\int_{\cos \lambda_0}^1 t^7 \left[\left(\frac{t^6}{\sqrt{4-3t^2}} \right)^{\frac{A+1}{2}} - (0.565)^{A+1} \right] dt$$

179
180 When integrating over equatorial pitch-angles α_0 , Liouville's theorem and the conservation of
181 the first adiabatic invariant (μ) are taken into account: $\sin^2 \alpha_{01} = B_0(L)/B(L, \lambda_0)$ and $\sin^2 \alpha_{02} =$
182 $B_0(L)/B(L, \lambda)$, where $B(L, 0) = B_0(L)$.

183 With an increase λ from 0 to $\lambda_0 = 30^\circ$, the value of the function $\sqrt{4-3t^2}$ increases from 1 to
184 1.32, i.e. deviates from the average value (1.16) by only 16%. Most part of the ERB protons are
185 concentrated at these latitudes. Therefore, when calculating the last integral, we will assume that
186 $\sqrt{4-3t^2} \approx 1.16$.

187 Then you can get the following expression:

$$\Delta N(L, f_d) = k \frac{J(L, E(L, f_d))}{\sqrt{E(L, f_d)}} F(A) L^2 dL dE,$$

188 where

$$F(A) = \frac{1}{A+1} \left[\frac{(1.16)^{-(A+1)/2}}{3A+11} (1 - 0.21 \cdot 0.65^A) - 0.085 (0.565)^{A+1} \right]$$

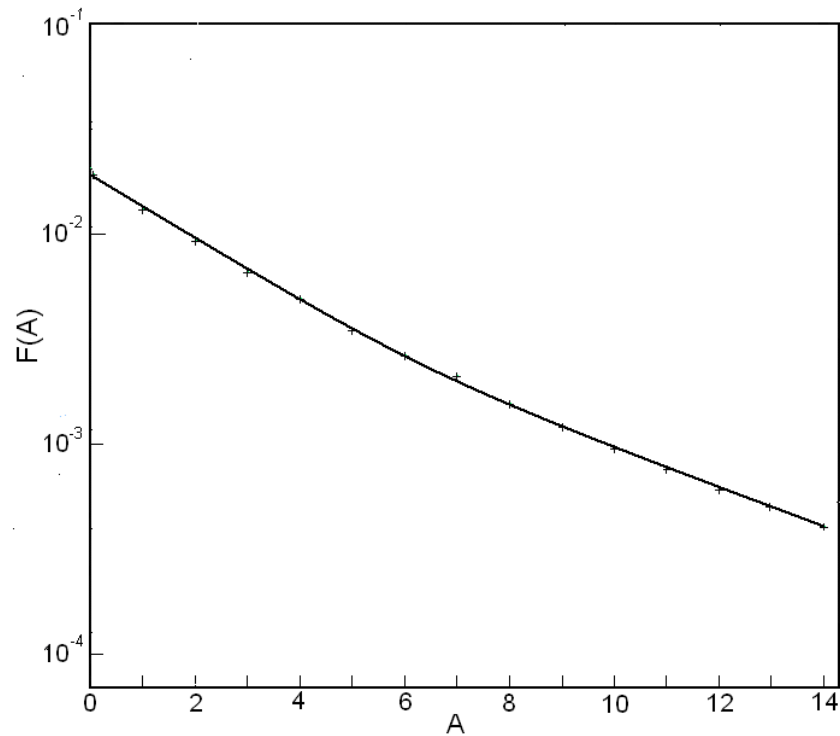
189 and

$$k = (4\pi)^2 R_E^3 \sqrt{m/2} = 2.945 \cdot 10^{19} \text{ cm}^2 \text{ s sr MeV}^{1/2}.$$

194 When calculating the values of ΔN , we will take that $dL/L = dE/E = 0.1$. Finally, for the
195 indicated ERB region near the equatorial plane, we obtain:

$$\Delta N(L, f_d) = 2.945 \cdot 10^{17} J(L, E(L, f_d)) \sqrt{E(L, f_d)} F(A) L^3, \quad (1)$$

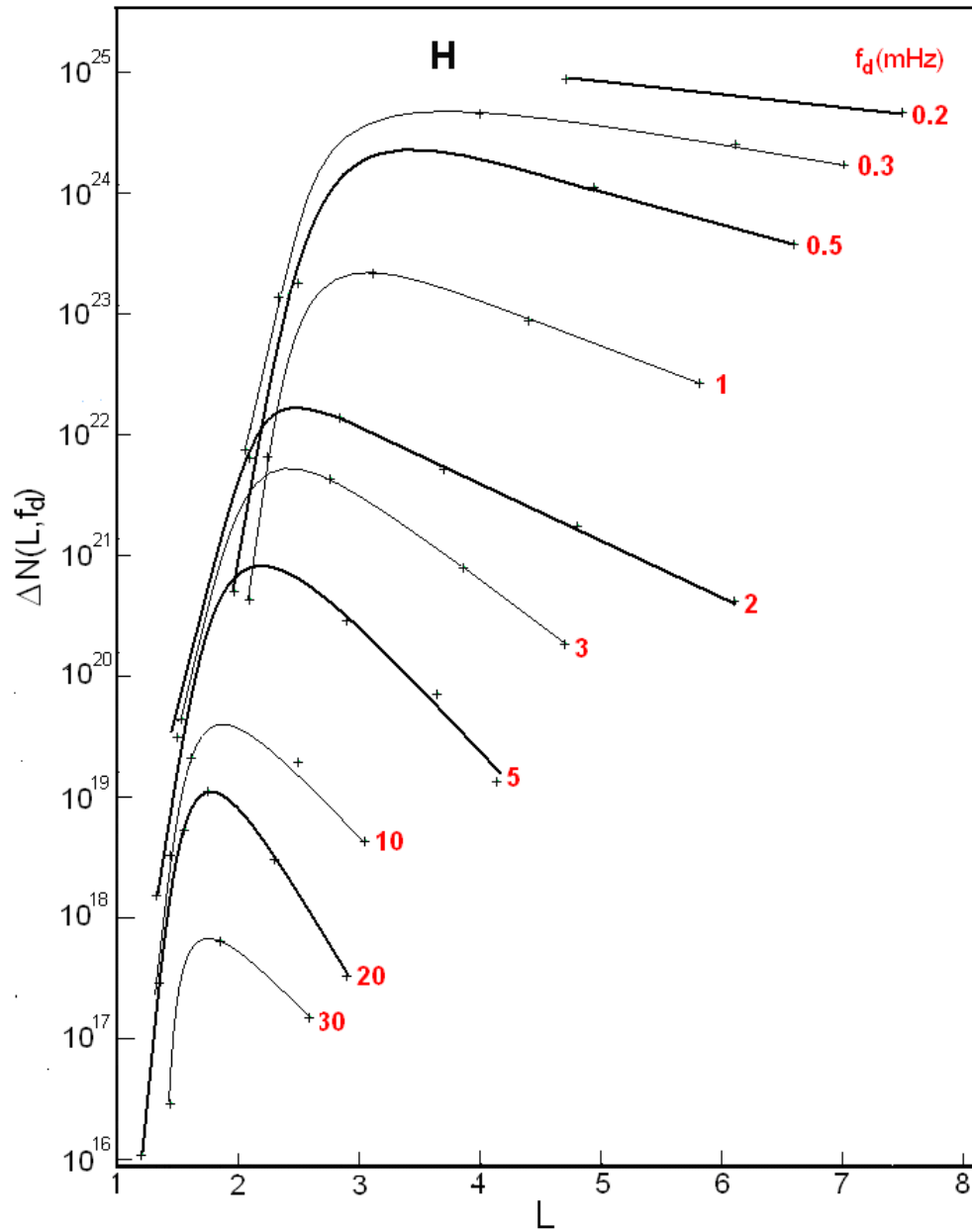
197 where J , the differential fluxes of protons with equatorially pitch-angle $\alpha_0 \approx 90^\circ$, is given in units
198 of $(\text{cm}^2 \text{ s sr MeV})^{-1}$, and the energy of protons E is given in MeV. The dependence $F(A)$ is shown
199 in Fig. 3.



200

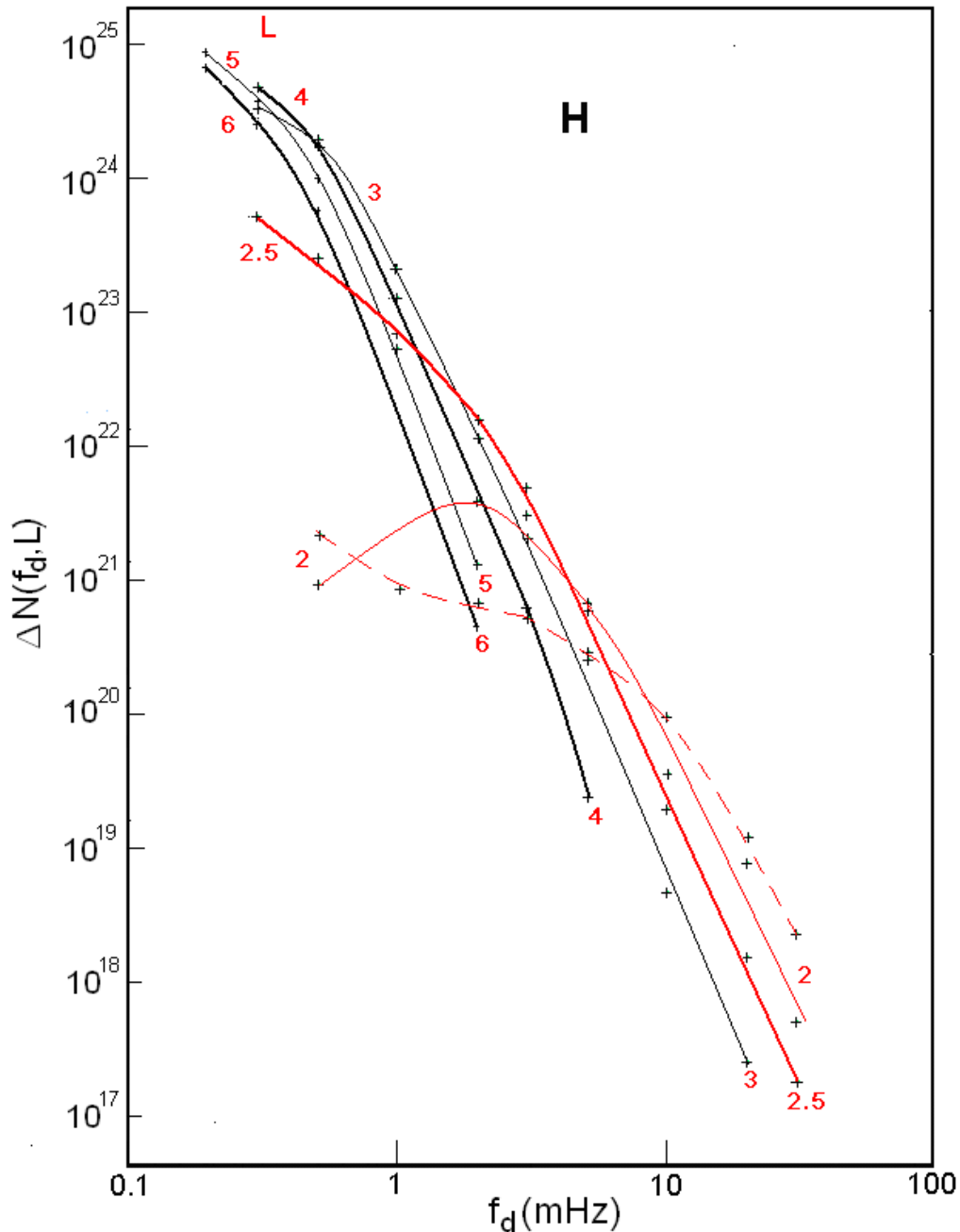
201 **Figure 3.** Dependence of the factor $F(A)$ in formula (1) on the anisotropy index A of the proton fluxes.

202 For protons of the ERB, the radial profiles $\Delta N(L, f_d)$ for $f_d = 0.2, 0.3, 0.5, 1, 2, 3, 5, 10, 20,$ and
 203 30 mHz, calculated using the formula (1) together with Figs. 1–3 are shown in Fig. 4, and the
 204 frequency spectra $\Delta N(f_d, L)$ at $L = 2, 2.5, 3, 4, 5,$ and 6 are shown in Fig. 5. Near each curve in Fig.
 205 4, the corresponding value of f_d (mHz) is indicated, and each spectrum in Fig. 5 have the
 206 corresponding L value (these values are highlighted in red). For clarity, in Figs. 4 and 5, thin
 207 curves alternate with thick curves and in Fig. 5 spectra at $L = 2$ and 2.5 are highlighted in red.



208

209 **Figure 4.** Radial profiles $\Delta N(L, f_d)$ for protons of the ERB with drift frequencies $f_d = 0.2, 0.3, 0.5, 1, 2, 3, 5, 10, 20$ and
 210 30 mHz, plotted for periods of **maximum** activity. The f_d values corresponding to each curve are highlighted in red. For
 211 clarity, thin curves are interspersed with thick curves.



212

213

214

215

216

Figure 5. Frequency spectra $\Delta N(f_d, L)$ for protons of the ERB at $L = 2, 2.5, 3, 4, 5$ and 6 , plotted for periods of **maximum** solar activity. The values L corresponding to each spectrum and spectra at $L = 2$ and 2.5 are highlighted in red. The red dotted line shows the spectrum $\Delta N(f_d, L)$ of the ERB protons at $L = 2$, constructed from data **during minimum** periods of solar activity (see Kovtyukh, 2020). For clarity, thin curves are interspersed with thick curves.

217

218

219

The errors of these calculations consist mainly of the errors of the averaged experimental data shown in Figs. 1 and 2 (these errors are most significant at $L < 2$), and because of the deviations of the geomagnetic field from the dipole model at $L > 5$.

220

221

222

223

224

As λ_0 decreases, the errors in our calculations will decrease. These errors can be reduced also by using numerical computer calculations. However, it should be taken into account that the fluxes of the ERB protons, as well as the energy spectra and pitch-angle distributions of these fluxes, may experience changes that exceed the errors of our calculations even in very quiet periods of observations.

225 3 Discussion

226 In agreement with the results of experimental and theoretical studies, at $L > 2.5$, the main
 227 mechanism for the formation of the ERB protons is the radial diffusion of particles from the outer
 228 boundary of the geomagnetic trap to the Earth under conservation the adiabatic invariants μ and K
 229 (see, e.g., Lejosne and Kollmann, 2020; Kovtyukh, 2016b, 2018).

230 Figs. 1 and 2 presented here make it possible to determine in which regions of the space $\{E, L\}$
 231 near the equatorial plane the ionization losses of ions during their radial diffusion can be neglected
 232 and where this cannot.

233 The iso-lines of proton fluxes in Fig. 1 at sufficiently large E and L go up with decreasing L , in
 234 the direction of increasing energy, in strict agreement with the adiabatic laws of radial transport of
 235 particles. At lower L these iso-lines **do change the direction of their course**, under the influence of
 236 ionization losses, which increase rapidly with decreasing L (see in Kovtyukh, 2020 for details).

237 At sufficiently large values of E and L , iso-lines of the anisotropy index in Fig. 2 pass
 238 practically parallel to each other and parallel to the energy axis, in agreement with the laws of
 239 adiabatic transport of particles with power-law energy spectra (see Kovtyukh, 1993). At lower E
 240 and L , a more complex picture is formed under the influence of ionization losses (for more details
 241 see in Kovtyukh, 2001, 2018).

242 With decreasing L , the radial diffusion **is** decreased very rapidly, and the belt of protons with E
 243 $> 10\text{--}20$ MeV on $L < 2$ is generated mainly as result of decay of neutrons of albedo which are
 244 knocked from the atmospheric atoms nuclei by the Galactic Cosmic Rays (GCR) protons. This
 245 mechanism (CRAND) is simulated in many contemporary studies based on the experimental data
 246 (see, e. g., Selesnick et al., 2007, 2013, 2014, 2018).

247 The mechanisms of formation of the ERB under the action of radial diffusion and CRAND are
 248 manifested and clearly differ both in the radial profiles $\Delta N(L, f_d)$ and in the frequency spectra
 249 $\Delta N(f_d, L)$ of protons.

250 Let us consider the manifestations of these mechanisms in Fig. 4 and 5 and related effects.

251 In contrast to the radial profiles of fluxes $J(L, E)$, the radial profiles $\Delta N(L, f_d)$ for protons with f_d
 252 > 10 mHz (see Fig. 4) have much less **steeper** outer edges and their steepness decreases with
 253 decreasing frequency f_d . This effect is connected mainly with an increase in the volume of
 254 magnetic tubes (factor L^3 in formula (1) from Section 2.3) and with a decrease in the anisotropy
 255 index of proton fluxes with increasing L .

256 At the same time, in comparison with the radial profiles $J(L, E)$, the radial profiles $\Delta N(L, f_d)$
 257 have more steeper inner edges. This effect is **mainly** connect **to** the large anisotropy of proton
 258 fluxes in the corresponding region of space $\{E, L\}$ and with the rapid growth of the anisotropy
 259 index with decreasing L in this region. It is especially expressed in the radial profiles $\Delta N(L, f_d)$ at f_d
 260 $\sim 0.3\text{--}1$ mHz (see Fig. 4); this is due to the fact that in the corresponding region of space $\{E, L\}$ the
 261 anisotropy index of proton fluxes strongly depends on E and L (see Fig. 2).

262 Radial profiles $\Delta N(L, f_d)$ at $f_d > 10$ mHz are formed by the mechanism CRAND. They have a
 263 maximum at $L \sim 1.5\text{--}2.0$, and the steepness of their inner and outer edges does not differ as much
 264 as for lower frequencies f_d (see Fig. 4). When constructing these profiles, it was taken into account
 265 that at $E = 5\text{--}50$ MeV an anisotropy index A of proton fluxes do not depend on L at $L = 1.25\text{--}1.40$:
 266 $A = 12 \pm 2$ (Fischer et al., 1977; Leonov et al., 2005).

267 The shape of the spectra $\Delta N(f_d, L)$ at $L > 3$ is determined, first of all, by the shape of the energy
 268 spectra of proton fluxes $J(E, L)$ at the outer boundary of the geomagnetic trap. Gradually, as the
 269 particles diffuse to the Earth, their energy spectra are transformed under the action of betatron
 270 acceleration and ionization losses of particles.

271 In contrast to the energy spectra of proton fluxes $J(E, L)$, distributions $\Delta N(f_d, L)$ of the ERB
 272 protons over their drift frequency f_d (Fig. 5) differ much less from each other at $L > 3$. Such
 273 convergence of the spectra $\Delta N(f_d, L)$ is driven by increase in the volume of magnetic tubes and a
 274 decrease in the anisotropy index of the ERB proton fluxes with increasing L . Fig. 5 demonstrates
 275 the closeness to the adiabatic transformations of the spectra $\Delta N(f_d, L)$ when L changes at $L > 3$.

276 The energy spectra of near-equatorial proton fluxes $J(E, L)$ with $E > 10 \cdot L^{-3}$ MeV at $L > 3$ in
 277 quiet periods have a local maximum at $E = (17 \pm 3) \cdot L^{-3}$ MeV and a power-law tail ($J \propto E^{-\gamma}$, where γ
 278 $= 4.25 \pm 0.75$) at $E > (36 \pm 11) \cdot L^{-3}$ (Kovtyukh, 2001, 2018, 2020).

279 The frequency spectra of the ERB protons at $L > 3$ weakly depend on L and over the considered
 280 range Δf_d have a close to power-law shape with an exponent $\gamma = 4.71 \pm 0.43$ (at $f_d > f_d^*$, where f_d^*
 281 ~ 0.5 mHz at $L \sim 3-6$, ~ 2 mHz at $L = 2.5$ and ~ 5 mHz at $L = 2$). Note that the spread of the
 282 parameter γ for the frequency spectra of protons is almost 2 times less than for their energy spectra.
 283 These spectra become more rigid (flattened) at $f_d < f_d^*$.

284 Thus, the average exponents of the power-law tail of the energy and frequency spectra of
 285 protons differ by $\Delta\gamma = 0.46$, and there is no local maximum in the frequency spectra at $f_d > 2$ mHz
 286 at $L > 2.5$. The main role in such differences in the shape of the energy and frequency spectra of
 287 protons was played by the factor $F(A)$ in formula (1), in which the anisotropy index A is a function
 288 of E and L (see Figs. 2 and 3). Note that in the region $\{E > 0.5 \text{ MeV}, L > 3\}$ the anisotropy index
 289 A , as well as the protons energy, is transformed according to adiabatic laws when L changes (see
 290 Fig. 2 and comments to it).

291 These results confirm our hypothesis about the ordering of the distributions of protons over
 292 their drift frequency f_d in the outer regions of the ERB, at $L > 3$, where most of the ERB protons
 293 are located and where the radial diffusion of protons overpowers their ionization losses.

294 At all L , the frequency spectra $\Delta N(f_d, L)$ become more flat at small f_d and E under influence
 295 ionization losses. However, in the range of high f_d (from 3–5 mHz to 30 mHz), for protons with
 296 high energies and low ionization losses, the protons frequency spectra have a power-law tail even
 297 at $L = 2$ (see Fig. 5).

298 For protons with $f_d < 0.5$ mHz, which correspond to the ERB protons of the lowest energies,
 299 ionization losses lead to the same consequences at higher L -shells: the radial profiles $\Delta N(L, f_d)$
 300 approach each other, and the spectra $\Delta N(f_d, L)$ flatten out (see Figs. 4 and 5).

301 In the region of the steep inner edge of the radial distributions $\Delta N(L, f_d)$, spectra $\Delta N(f_d, L)$ of the
 302 ERB protons become gradually increasingly rigid with decreasing L , and rapidly diverge from each
 303 other (see Fig. 4 and 5). In the range of small f_d at $L < 2.5$, the connection between these
 304 distributions and the shape of the boundary energy spectra of protons is gradually lost.

305 These results indicate a violation of the order in the distributions of protons under the influence
 306 of ionization losses.

307 According to numerous experimental data, during magnetic storms, a wide variety of complex
 308 spectra of powerful pulsations of magnetic and electric fields in the considered frequency range
 309 (ULF) can be generate in the geomagnetic trap, which are non-regularly distributed over L ; these
 310 pulsations can lead to local acceleration and losses of the ERB particles (see, e.g., Sauvaud et al.,
 311 2013). Such effects will violate the regular characteristics of the protons distributions shown in
 312 Fig. 4 and 5. However, during quiet periods, the amplitudes of such pulsations are small and they
 313 lead only to radial diffusion of particles.

314 In Fig. 5, the dotted line also shows the spectrum $\Delta N(f_d, L)$ of the ERB protons at $L = 2$,
 315 constructed from experimental data for periods of low solar activity (see Fig. 1 in Kovtyukh,

2020). Fig. 5 show that at $L = 2$ for $f_d > 10$ mHz there were more protons at the minimum of solar activity, and for $f_d \sim 1-10$ mHz there were more protons at the maximum of solar activity.

The effect of a decrease in the $\Delta N(f_d, L)$ values for protons with $f_d > 10$ mHz at $L < 2$ with an increase in solar activity is mainly connected with a decrease in the fluxes of protons with $E > 10-20$ MeV here. This effect is well known. It is described by the CRAND mechanism (see, e.g., Selesnick et al., 2007) and was considered in detail in (Kovtyukh, 2020). With an increase in solar activity, the densities of atmospheric atoms and ionospheric plasma on small L -shells significantly increase, which leads to an increase in ionization losses of the ERB protons, but the power of their main source (CRAND) practically does not change. As a result, the equilibrium fluxes and $\Delta N(f_d, L)$ for protons with $f_d > 10$ mHz are established at lower levels.

However, the effect of an increase in $\Delta N(f_d, L)$ for $f_d \sim 1-10$ mHz at low L with increasing solar activity, corresponding to the protons of lower energies, was discovered here for the first time.

With decreasing E (and f_d) of protons their ionization losses increase, and if the fluxes of low-energy protons in the inner belt were also formed by the CRAND mechanism, one would have observed even stronger increase of their fluxes with decreasing solar activity, than for protons with $E > 10-20$ MeV ($f_d > 10$ mHz). But for protons with $f_d \sim 1-10$ mHz, we see in Fig. 5 the opposite effect in the spectra $\Delta N(f_d, L)$ at $L = 2$, which is not described by the CRAND mechanism.

On the other hand, it was proved that stationary fluxes of protons with $E < 15$ MeV at $L \sim 2$ are formed mainly by the mechanism of protons radial diffusion from the external region of the ERB (Selesnick et al., 2007, 2013, 2014, 2018). These fluxes and $\Delta N(f_d, L)$ values for $f_d \sim 1-10$ mHz at $L = 2$ are formed as a result of a balance of competing processes radial diffusion of protons and their ionization losses.

The rates of transport of the ERB protons to the Earth (radial diffusion) rapidly increase with decreasing particles energy (see Kovtyukh, 1916b). In addition, with an increase in solar activity, the average level of geomagnetic fluctuations in the ERB increases. Under the influence of these factors, one can expect a significant increase in the intensity of radial diffusion of the low-energy protons at low L with an increase in solar activity. As a result, the effect of increasing in the density of a dissipative medium with an increase in solar activity is overpowered by a more significant effect of increasing in the rates of radial diffusion of protons.

4 Conclusions

Starting from the data on near-equatorial ERB proton fluxes (with energy from 0.2 to 100 MeV and drift L shells ranging from 1 to 8), their stationary distributions over the drift frequency of particles around the Earth (f_d) were constructed. The results of calculations of the number ΔN of the ERB protons within 30° in geomagnetic latitude at different L and f_d for periods of maximum solar activity are presented. They differ from the corresponding distributions of the ERB protons for periods of low solar activity only at $L < 2.5$ (for comparison, the spectra of these distributions are given at $L = 2$).

The radial profiles of these distributions $\Delta N(L, f_d)$ have only one maximum that shifts toward the Earth with increasing f_d . In comparison to the proton fluxes profiles $J(L, E)$, the radial profiles $\Delta N(L, f_d)$ at $f_d < 5$ mHz have steeper inner edges and flatter outer edges. However, the radial profiles $\Delta N(L, f_d)$ at $f_d > 10$ mHz, which are formed by the CRAND mechanism, have inner and outer edges with only slightly difference from each other for what concerns the steepness of their profiles.

In contrast to the energy spectra of proton fluxes $J(E, L)$, the frequency spectra $\Delta N(f_d, L)$ of the ERB protons at $L > 3$ are weakly dependent on L and, for sufficiently large f_d they have a nearly

361 power-law **shape** with an exponent $\gamma = 4.71 \pm 0.43$. There is no local maximum in these spectra
 362 in the region $\{f_d > 2 \text{ mHz}, L > 2.5\}$, as in the corresponding $J(E, L)$ spectra.

363 Distributions $\Delta N(L, f_d)$ and $\Delta N(f_d, L)$ of the ERB protons in the region $\{f_d > 0.5 \text{ mHz}, L > 3\}$
 364 have a more **regular shape** than in the corresponding region of the space $\{E, L\}$, and the main
 365 physical processes in the ERB manifested more clearly in these distributions. In these regions,
 366 **there is the majority** of the ERB protons, and **their** radial diffusion overpowers their ionization
 367 losses during the transport of particles to the Earth.

368 In the region of the steep inner edges of the radial distributions $\Delta N(L, f_d)$, the spectra $\Delta N(f_d, L)$
 369 of protons rapidly diverge from each other with decreasing L , and at low frequencies these spectra
 370 become flatten. These results indicate a violation of the order in these distributions of protons
 371 under the influence of ionization losses.

372 With increasing solar activity, the number of protons $\Delta N(f_d, L)$ at $L \sim 2$ decreases for $f_d > 10$
 373 mHz and increases for $f_d \sim 1\text{--}10$ mHz. The effect at high f_d , corresponding to protons with $E > 15$
 374 MeV, is well known and is described in the framework of the CRAND mechanism.

375 However, the opposite effect, at low f_d corresponding to the lower-energy protons, is discovered
 376 here for the first time. This effect can be associated with the fact that the low-frequency part of the
 377 spectrum $\Delta N(f_d, L)$ of protons, even at $L \sim 2$, is **mainly** formed by the mechanism of protons
 378 transport from the outer regions of the ERB. This effect may indicate that with increasing solar
 379 activity, the average rates of radial diffusion of protons increase **as well**. For low-energy protons at
 380 $L \sim 2$, the effect of increasing density of a dissipative medium with increasing solar activity **is**
 381 overpowered by **the increase of** the rates of radial diffusion of particles.

382

383 *Data availability.* All data from this investigation are presented in Figs. 1–5.

384 *Competing interests.* The author declares that there is no conflict of interest.

385 *Acknowledgements.* The author would like to thank the reviewers.

386

387

388 **References**

- 389 Alfvén, H., and Fälthammar, C.-G.: *Cosmical Electrodynamics, Fundamental Principles*,
390 Clarendon Press, Oxford, 1963.
- 391 Davis, L. R.: Low energy trapped protons and electrons, *Proc. Plasma Space Sci. Symp.*, Eds. D.
392 B. Chang and C. Y. Huang, Washington, P. 212–226, 1965.
- 393 Fennell, J. F., Blake, J. B., and Paulikas, G. A.: Geomagnetically trapped alpha particles, 3. Low-
394 altitude outer zone alpha-proton comparisons, *J. Geophys. Res.*, **79**(4), 521–528,
395 <https://doi.org/10.1029/JA079i004p00521> , 1974.
- 396 Fischer, H. M., Auschrat, V. W., and Wibberenz, G.: Angular distribution and energy spectra of
397 protons of energy $5 \leq E \leq 50$ MeV in the lower edge of the radiation belt in equatorial latitudes,
398 *J. Geophys. Res.*, **82**(4), 537–547, <https://doi.org/10.1029/JA082i004p00537>, 1977.
- 399 Fritz, T. A., and Spjeldvik, W. N.: Steady-state observations of geomagnetically trapped energetic
400 heavy ions and their implications for theory, *Planet. Space Sci.*, **29**(11), 1169–1193,
401 [https://doi.org/10.1016/0032-0633\(81\)90123-9](https://doi.org/10.1016/0032-0633(81)90123-9), 1981.
- 402 Garcia, H. A., and Spjeldvik, W. N.: Anisotropy characteristics of geomagnetically trapped ions, *J.*
403 *Geophys. Res.*, **90**(A1), 359–369, <https://doi.org/10.1029/JA090iA01p00359>, 1985.
- 404 Hoffman, R. A., and Bracken, P. A.: Magnetic effects of the quiet-time proton belt, *J. Geophys.*
405 *Res.*, **70**(15), 3541–3556, <https://doi.org/10.1029/JZ070i015p03541> , 1965.
- 406 Ilyin, B. D., Kuznetsov, S. N., Panasyuk, M. I., and Sosnovets, E. N.: Non-adiabatic effects and
407 boundary of the trapped protons in the Earth's radiation belts, *Bulletin of the Russian Academy*
408 *of Sciences: Physics*, **48**(11), 2200–2203, 1984.
- 409 Kovtyukh, A. S.: Relation between the pitch-angle and energy distributions of ions in the Earth's
410 radiation belts, *Geomagn. Aeron.*, **33**(4), 453–460, 1993.
- 411 Kovtyukh, A. S.: Geocorona of hot plasma, *Cosmic Res.*, **39**(6), 527–558,
412 <https://doi.org/10.1023/A:1013074126604>, 2001.
- 413 Kovtyukh, A. S.: Radial dependence of ionization losses of protons of the Earth's radiation belts,
414 *Ann. Geophys.*, **34**(1), 17–28, <https://doi.org/10.5194/angeo-34-17-2016>, 2016a.
- 415 Kovtyukh, A. S.: Deduction of the rates of radial diffusion of protons from the structure of the
416 Earth's radiation belts, *Ann. Geophys.*, **34**(11), 1085–1098, <https://doi.org/10.5194/angeo-34-1085-2016>, 2016b.
- 418 Kovtyukh, A. S.: Ion Composition of the Earth's Radiation Belts in the Range from 100 keV to
419 100 MeV/nucleon: Fifty Years of Research, *Space Sci. Rev.*, **214**(8), 124:1–124:30,
420 <https://doi.org/10.1007/s11214-018-0560-z>, 2018.
- 421 Kovtyukh, A. S.: Earth's radiation belts' ions: patterns of the spatial-energy structure and its solar-
422 cyclic variations, *Ann. Geophys.*, **38**(1), 137–147, doi:10.5194/angeo-38-137-2020, 2020.
- 423 Lejosne, S., and Kollmann, P.: Radiation Belt Radial Diffusion at Earth and Beyond, *Space Sci.*
424 *Rev.*, **216**(1), 19:1–19:78, <https://doi.org/10.1007/s11214-020-0642-6>, 2020.
- 425 Leonov, A., Cyamukungu, M., Cabrera, J., Leleux, P., Lemaire, J., Gregorie, G., Benck, S.,
426 Mikhailov, V., Bakaldin, A., Galper, A., Koldashov, S., Voronov, S., Casolino, M., De Pascale,
427 M., Picozza, P., Sparvulli, R., Ricci, M.: Pitch-angle distribution of trapped energetic protons
428 and helium isotop nuclei measured along the Resurs-01 No.4 LEO satellite, *Ann. Geophys.*,
429 **23**(8), 2983–2987, <https://doi.org/10.5194/angeo-23-2983-2005>, 2005.
- 430 Northrop, T. G.: *The Adiabatic Motion of Charged Particles*, Wiley-Interscience, NY, USA, 1963.
- 431 Parker, E. N.: Newtonian development of the dynamical properties of ionized gases of low density,
432 *Phys. Rev.*, **107**(4), 924–933. <https://doi.org/10.1103/PhysRev.107.924>, 1957.
- 433 Roederer, J. G.: *Dynamics of Geomagnetically Trapped Radiation*, Springer, NY, USA, 1970.
- 434 Sauvaud, J.-A., Walt, M., Delcourt, D., Benoist, C., Penou, E., Chen, Y., and Russell C. T.: Inner
435 radiation belt particle acceleration and energy structuring by drift resonance with ULF waves

- 436 during geomagnetic storms, *J. Geophys. Res. Space Physics*, **118**(4), 1723–1736,
437 <https://doi.org/10.1002/jgra.50125>, 2013.
- 438 Selesnick, R. S., Looper, M. D., and Mewaldt, R. A.: A theoretical model of the inner proton
439 radiation belt, *Space Weather*, **5**(4), S04003, <https://doi.org/10.1029/2006SW000275>, 2007.
- 440 Selesnick, R. S., Hudson, M. K., and Kress B. T.: Direct observation of the CRAND proton
441 radiation belt source, *J. Geophys. Res. Space Phys.*, **118**(12), 7532–7537,
442 <https://doi.org/10.1002/2013JA019338>, 2013.
- 443 Selesnick, R. S., Baker, D. N., Jaynes, A. N., Li, X., Kanekal, S. G., Hudson, M. K., and Kress, B.
444 T.: Observations of the inner radiation belt: CRAND and trapped solar protons, *J. Geophys.
445 Res. Space Phys.*, **119**(8), 6541–6552, <https://doi.org/10.1002/2014JA020188>, 2014.
- 446 Selesnick, R. S., Baker, D. N., Kanekal, S. G., Hoxie, V. C., and Li, X.: Modeling the proton
447 radiation belt with Van Allen Probes Relativistic Electron-Proton Telescope data, *J. Geophys.
448 Res. Space Phys.*, **123**(1), 685–697, <https://doi.org/10.1002/2017JA024661>, 2018.
- 449 Shi, R., Summers, D., Ni, B., Manweiler, J. W., Mitchell, D. G., and Lanzerotti, L. J.: A statistical
450 study of proton pitch-angle distributions measured by the Radiation Belt Storm Probes Ion
451 Composition Experiment, *J. Geophys. Res. Space Phys.*, **121**(6), 5233–5249,
452 <https://doi.org/10.1002/2015JA022140>, 2016.
- 453 Søråas, F., and Davis, L.R.: Temporal variations of 100 keV to 1700 keV trapped protons observed
454 on satellite Explorer 26 during first half of 1965, Rep. X-612-68-328, NASA Goddard Space
455 Flight Cent., Greenbelt, Md., 1968.
- 456 Williams, D. J., and Lyons, L. R.: The proton ring current and its interaction with plasmapause:
457 Storm recovery phase, *J. Geophys. Res.*, **79**(28), 4195–4207,
458 <https://doi.org/10.1029/JA079i028p04195>, 1974.
- 459 Williams, D. J., and Frank, L. A.: Intense low-energy ion populations at low equatorial altitude, *J.
460 Geophys. Res.*, **89**(A6), 3903–3911, <https://doi.org/10.1029/JA089iA06p03903>, 1984.